

The Bulk-Hinge Correspondence and Three-Dimensional Quantum Anomalous Hall Effect in Second Order Topological Insulators

Bo Fu, Zi-Ang Hu, and Shun-Qing Shen*

Department of Physics, The University of Hong Kong, Pokfulam Road, Hong Kong, China

The chiral hinge modes are the key feature of a second order topological insulator in three dimensions. Here we propose a quadrupole index in combination of a slab Chern number in the bulk to characterize the flowing pattern of chiral hinge modes along the hinges at the intersection of the surfaces of a sample. We further utilize the topological field theory to demonstrate the correspondent connection of the chiral hinge modes to the quadrupole index and the slab Chern number, and present a picture of three-dimensional quantum anomalous Hall effect as a consequence of chiral hinge modes. The two bulk topological invariants can be measured in electric transport and magneto-optical experiments. In this way we establish the bulk-hinge correspondence in a three-dimensional second order topological insulator.

Introduction The bulk-boundary correspondence lies at the heart of topological states of matter and topological materials [1–4]. It bridges the topology of bulk band structures and the physical observables near the boundary. In the quantum Hall effect and quantum anomalous Hall effect (QAHE), the quantized Hall conductance is associated with the TKNN number of the band structure and the number of the edge modes of electrons around the boundary [5–8]. In a topological insulator, a Z_2 index in the bulk is associated with the number of the gapless Dirac cones of the surface electrons [9–11]. This reflects intrinsic attributes of the topological phenomena. A recent advance in the field of topological materials is the discovery of higher-order topological insulators [12–20]. A second-order topological insulator in three dimensions refers to an insulator with one-dimensional the chiral hinge modes (CHMs) localized on the hinges at the intersection of adjacent side surfaces [15–26]. Over the past few years, a great of efforts have been made to explore the possible relation of the bulk bands and existence of hinge modes as an extension of the bulk-boundary correspondence, such as effective mass analysis [18–23], the symmetry indicator [27–35], and spectral flow analysis [36]. All the approaches have their own merits. However, CHMs in a second order topological insulator may display various flowing patterns as illustrated in Fig. 1. It lacks a systematic method to provide a comprehensive description of diverse flowing patterns. Also it is desirable to learn which observable in the bulk is associated with the CHMs.

In this Letter, we address the bulk-hinge correspondence and three-dimensional (3D) QAHE as a physical consequence of the CHMs in a second-order topological insulator. We start with a minimal four-band model to reveal different flowing patterns of CHMs. It is found that a quadrupole index is associated with the flowing direction of four hinge modes of the system along one direction and a slab quantized Hall conductance reveals the formation of a closed loop of the CHMs. We further

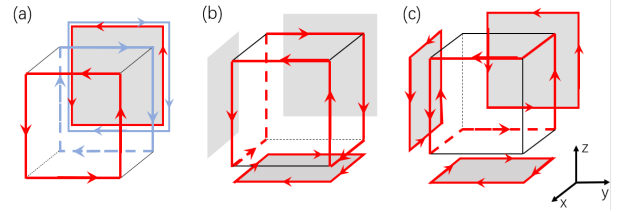


Figure 1. Illustration of selected patterns of chiral hinge modes and their projection in a second order topological insulator in three dimensions. (a) A double-loop pattern with the quadrupole indices $\Delta_{xy} = -\Delta_{zx} = 1$ and $\Delta_{yz} = 0$ and the slab Chern number $n_x = n_y = n_z = 0$. (b) A single-loop pattern with $\Delta_{xy} = 1$ and $\Delta_{yz} = \Delta_{zx} = 0$ and $n_x = n_y = 0$ and $n_z = -1$. (c) A single-loop pattern with $\Delta_{xy} = \Delta_{yz} = \Delta_{zx} = 0$ and $n_x = n_y = -n_z = 1$.

demonstrate the correspondent connection of the CHMs to the quadrupole index and the slab Chern number by means of topological field theory. Finally we propose to utilize magneto-optical Faraday and Kerr effects to detect these topological invariants.

Model Hamiltonian and symmetry analysis We start with a minimal four-band Hamiltonian, $\mathcal{H} = \mathcal{H}_0 + \sum_{i=1}^3 \mathcal{V}_i$, which consists of four parts. The first part is

$$\mathcal{H}_0 = \hbar\sigma_x[v_\perp(k_x s_x + k_y s_y) + v_z k_z s_z] + [m_0 + m_\perp(k_x^2 + k_y^2) + m_z k_z^2]\sigma_z s_0 \quad (1)$$

where k_x, k_y, k_z are the wave vectors, m_i and v_i are model parameters. \mathbf{s} and $\boldsymbol{\sigma}$ are the Pauli matrices acting in spin and orbital space, respectively. \mathcal{H}_0 possesses the time reversal symmetry \mathcal{T} ($\mathcal{T}^2 = -1$) and belongs to the symplectic symmetry class AII. Here we focus on the case of both $m_0 m_\perp < 0$ and $m_0 m_z < 0$ such that \mathcal{H}_0 describes a 3D strong topological insulator with gapless Dirac cone of the surface states at all surfaces [4, 38]. \mathcal{H}_0 also respects the global chiral symmetry $\mathcal{C} = \sigma_y s_0$, $\{\mathcal{C}, \mathcal{H}_0\} = 0$. Including the crystalline symmetries, the total point symmetry group is $\mathcal{G}_0 = D_{4h} \times \{1, \mathcal{T}, \mathcal{P}, \mathcal{C}\}$ with the particle-hole symmetry $\mathcal{P} \equiv \mathcal{C}\mathcal{T}^{-1}$ [37]. As shown below all the terms in \mathcal{H} preserve \mathcal{P} , it is more

* sshen@hku.hk

convenient to rewrite \mathcal{G}_0 as $\mathcal{G}_0 = \tilde{\mathcal{G}}_0 \times \{1, \mathcal{P}\}$ with the magnetic group $\tilde{\mathcal{G}}_0 = D_{4h} \times \{1, \mathcal{T}\} = D_{4h} \oplus \mathcal{T}D_{4h}$ (or $4/mmm1'$). $\mathcal{V}_1 = c(k_x^2 - k_y^2)\sigma_y s_0$ breaks the time reversal symmetry \mathcal{T} . The presence of \mathcal{V}_1 reduces magnetic group to $\tilde{\mathcal{G}}' = D_{2d} \oplus \mathcal{T}(D_{4h} - D_{2d})$. The term proportional to c opens a gap with opposite sign for the surface states on the neighboring surfaces parallel to z axis and the CHMs may be localized at their intersections. The CHMs are protected by the combination of four fold rotational symmetry and time-reversal symmetry $\mathcal{R}_4^z \mathcal{T}$. The surface states on the bottom (00 $\bar{1}$) and top (001) surface remain gapless. $\mathcal{V}_2 = d\sigma_y s_0$ and $\mathcal{V}_3 = \sum_{i=x,y,z} b_i s_i$ is the magnetic Zeeman interaction. The two terms $d\sigma_y s_0$ and $b_z \sigma_z s_z$ anticommute with the linear terms $\hbar v_\perp (k_x \sigma_x s_x + k_y \sigma_y s_y)$ along x and y directions. Thus they act as the mass terms and gap out the surface states on (001) and (00 $\bar{1}$) while being projected onto the x - y surface. Since both of them commute with the mass term $\sigma_y s_0$, so they only modifies the mass term for the surface states parallel with the z -axis and have no influences on the four hinge states along the z direction. When all the surface states are gapped out and the Fermi level is located in the surface band gap, the electrons can only propagate unidirectionally along the hinges shared by adjacent side surfaces due to time reversal symmetry breaking. However, with different parameters, the chiral hinge modes can exhibit distinctly different patterns. The presence of both \mathcal{V}_1 and \mathcal{V}_2 reduces the magnetic group to $\tilde{\mathcal{G}}_1 = D_2 \oplus \mathcal{T}(D_{2h} - D_2)$. The term proportional to d breaks both the time reversal \mathcal{T} and inversion symmetry \mathcal{I} , respectively, but respects the antiunitary combination \mathcal{IT} which means the fact that if one CHMs propagates along any hinge there must be another hinge state propagating in the same direction on its spatial inversion. Thus the CHMs may form two closed loops on the surfaces (100) and ($\bar{1}00$) as shown in Fig. 1(a). The relative sign between c in \mathcal{V}_1 and d in \mathcal{V}_2 will determine which surface the two hinge mode loops locate around.

The presence of both \mathcal{V}_1 and $\mathcal{V}_3 = b_z s_z$ with magnetic field in z direction reduces the magnetic group to $\tilde{\mathcal{G}}_2 = S_4 \oplus \mathcal{T}(D_{2d} - S_4)$. The term breaks the \mathcal{IT} symmetry while preserving the S_4 symmetry which protects a single-loop CHMs wriggling around the bulk as shown in Fig. 1(b). The relative sign between b and c determines the wriggling way of the single-loop CHMs. Only in the presence of $\mathcal{V}_3 = b \sum_{i=x,y,z} s_i$ that magnetic field points to (111) direction, the magnetic point group is $\tilde{\mathcal{G}}_3 = C_i \oplus \mathcal{T}(C_{2h} - C_i)$. Due to the presence of the inversion symmetry \mathcal{I} , the CHMs at the inversion symmetric hinges are propagating in the opposite directions, and form a closed loop as shown in Fig. 1(c). A detailed symmetry analysis can be found in Ref. ([39]).

Quadrupole index and slab Chern number In order to characterize the topological hinge modes, we introduce two topological invariants: the quadrupole index and slab Chern number. There are the CHMs along four hinges in the z direction in the case of Figs. 1(a) and (b). The

energy dispersions of the four hinge modes connect the conduction and valence bands, and cross at $k_z = 0$ (see Fig.S1 in [39]). For a specific k_z , $\mathcal{H}(k_z)$ can be viewed as a 2D system in the x - y plane and there are four corner states. The existence of corner states can be characterized by the quadrupole moment [40–42],

$$q_{xy}(k_z) = \frac{1}{2\pi} \text{Im} \log \left[\text{Det}[U_{k_z}^\dagger Q_{xy} U_{k_z}] \sqrt{\text{Det} Q_{xy}^\dagger} \right]$$

where the matrix U_{k_z} is constructed by the occupied lowest energy states, $Q_{xy} = e^{2\pi i \hat{r}_x \hat{r}_y / L_x L_y}$, \hat{r}_α are the position operators, and L_α are the lengths of the system in the α direction. Any anti-symmetry \mathcal{O}_a leaves xy plane invariant $\mathcal{O}_a \mathcal{H}(k_z) \mathcal{O}_a^{-1} = -\mathcal{H}(-k_z)$ will put a constraint on the quadrupole moment $q_{xy}(k_z)$: $q_{xy}(k_z) + q_{xy}(-k_z) = 0$ or 1 . At two high symmetry points $\Lambda_z = 0$ or π , the symmetry is restored, $\mathcal{O}_a \mathcal{H}(\Lambda_z) \mathcal{O}_a^{-1} = -\mathcal{H}(\Lambda_z)$, and $q_{xy}(\Lambda_z)$ must be quantized to 0 or $\frac{1}{2}$ (see Ref. [39]). Non-zero quantized $q_{xy}(\Lambda_z)$ indicates the system topologically nontrivial and the existence of four zero-energy corner states in the reduced 2D subspace. For example, if $q_{xy}(k_z = 0) = 1/2$, then $q_{xy}(\pm\pi) = 0$ or 1 . In this case, there exist CHMs which compensate for the difference of the corner charges. Thus we can introduce a quadrupole index,

$$\Delta_{xy} = \int_0^{2\pi} dk_z \partial_{k_z} q_{xy}(k_z) \quad (2)$$

to characterize the existence and the flowing direction of four CHMs. For the double-loop case in Fig. 1(a), we have $\Delta_{xy} = -\Delta_{zx} = 1$ and $\Delta_{yz} = 0$, which are protected by the combination of chiral symmetry and the mirror symmetry \mathcal{CM}_α and the combination of chiral symmetry and the time reversal symmetry \mathcal{CT} . For the single-loop case in Fig. 1(b), we have $\Delta_{xy} = 1$ and $\Delta_{yz} = \Delta_{zx} = 0$. The quadrupole index along the z direction is protected only by \mathcal{CT} and along the x (y) is protected by both $\mathcal{CM}_{x(y)}$ and \mathcal{CT} . For the case in Fig. 1(c), $\Delta_{xy} = \Delta_{yz} = \Delta_{zx} = 0$.

The slab Chern number is another topological invariant as the quadrupole index alone are not enough to characterize the diversity of the flowing pattern of the CHMs. Consider a slab geometry of the sample with a finite thickness L_z with the periodic boundary condition along the x and y direction. Denote the Bloch eigenstates by $|u_n(\mathbf{k}_\perp, z)\rangle$ are the Bloch eigenstates, $\mathcal{H}(\mathbf{k}_\perp, z)|u_n(\mathbf{k}_\perp, z)\rangle = \varepsilon_n(\mathbf{k}_\perp)|u_n(\mathbf{k}_\perp, z)\rangle$ with $\mathbf{k}_\perp = (k_x, k_y)$ and the index n for the bands. The space-resolved Berry connection is given by $\mathcal{A}_{\alpha;n,n'}(\mathbf{k}_\perp, z) = -i\langle u_n(\mathbf{k}_\perp, z)|\partial_\alpha|u_{n'}(\mathbf{k}_\perp, z)\rangle$ for the two occupied bands n, n' . In this way we define the slab Hall conductance and its relation to a slab Chern number n_z [35]

$$\sigma_{xy}^{slab} = \int_0^{L_z} dz \sigma_{xy}(z) = n_z \frac{e^2}{h} \quad (3)$$

where $\sigma_{xy}(z) = \frac{e^2}{2\pi h} \int d^2 \mathbf{k}_\perp \text{Tr}[\mathcal{F}_{xy}(\mathbf{k}_\perp, z)]$ and $\mathcal{F}_{xy}(\mathbf{k}_\perp, z)$ is the non-Abelian Berry curvature in terms of $\mathcal{A}_{\alpha; n, n'}(\mathbf{k}_\perp, z)$. Because of the periodicity of the Berry connection in the first Brillouin zone, it can be proved that the slab Chern number n_z is quantized if the filled bands has a band gap to the excited states for a band insulator. According to the bulk-boundary correspondence [8], each non-zero Chern number is associated with the closed loop of chiral edge state. In Fig. 1(a), $n_x = n_y = n_z = 0$, while two quadrupole indices are not vanishing $\Delta_{xy} = -\Delta_{zx} = 1$. The system in a slab geometry (the open boundary condition is imposed in the y direction) is analogue to the quantum spin Hall insulator except the the two counter-propagating hinges modes are localized on the opposite sides. Experimentally, the quantized anomalous Hall effect can be measured by using the surface-sensitive method [43]. In Fig. 1(b), $n_z = -1$ and $n_x = n_y = 0$. There is a closed loop of chiral edge mode around the z axis. Combined with the non-zero quadrupole index $\Delta_{xy} = 1$. there are four CHMs along the four hinges along the z axis, the two indices can determine that a single-loop of CHMs that wriggles around the bulk. QAHE can be detected through a global quantum Hall measurement probing the whole sample due to the nonzero n_z . In Fig. 1(c), $n_x = n_y = -n_z = 1$. There is a single loop of chiral edge mode around each axis. Because of the zero quadrupole indices around the three axis, there is no four CHMs along one direction. It exhibits a single CHM traversing half of its hinges, which can be projected out a single closed loop in the direction of x , y and z . The QAHE can be observed for three directions due to the non vanishing slab Chern numbers.

3D QAHE The CHMs can be further understood in the framework of topological field theory with an effective action[44],

$$\mathcal{S} = \int d^3 r dt \left[\frac{1}{8\pi} \left(\epsilon \mathbf{E}^2 - \frac{1}{\mu} \mathbf{B}^2 \right) + \frac{\theta(\mathbf{r}, t) e^2}{4\pi^2 \hbar c} \mathbf{E} \cdot \mathbf{B} \right], \quad (4)$$

where \mathbf{E} and \mathbf{B} are the electromagnetic fields, ϵ and μ are the dielectric constant and magnetic permeability, respectively. $\theta(\mathbf{r}, t)$ is known as the axion angle[45]. The product $\mathbf{E} \cdot \mathbf{B}$ is odd under the time reversal or spatial inversion, θ has to be 0 (modulo 2π) for a trivial insulator and the vacuum and π for a topological insulator with respect to the symmetries[39, 46, 47]. In the quadratic order of electric and magnetic fields, besides the Maxwell term, the θ term may give rise to the topologically magneto-electric effect that an electric field can induce a magnetic field and vice verse[44, 48, 50–52]. By taking the functional derivative of θ term with respect to a gauge field, the induced electric current density depends on the spatial and temporal gradients of the θ -field[44, 45],

$$\mathbf{j}_\theta(\mathbf{r}, t) = \frac{e^2}{2\pi h} [\partial_t \theta(\mathbf{r}, t) \mathbf{B} - \nabla \theta(\mathbf{r}, t) \times \mathbf{E}]. \quad (5)$$

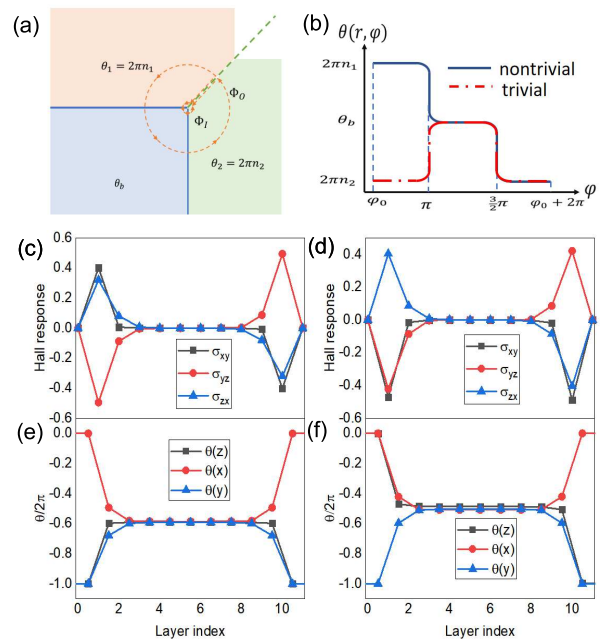


Figure 2. (a) Schematic view of the hinge current. The planar surfaces of the topological insulator are characterized by integers n_1 and n_2 , describing the integer change of the θ value nearby the surfaces. (b) Schematic view of θ -term as a function of the angle φ for topologically nontrivial and trivial cases. (c) and (d) Plots of the layer-resolved Hall response $\sigma_{\alpha\beta}(r_\gamma)$ and (e) and (f) plots of the θ -angle as function of the layer index for two cases phases from a layer-resolved Kubo formula in a slab geometry for 10 layers.

The first term depends on the temporal gradient of the θ -field and is proportional to magnetic field, i.e., the so-called chiral magnetic field, and vanishes in a static limit. The second term depends spatial gradient of the θ -field and is perpendicular to the electric field, i.e., the anomalous Hall effect. Thus there will be surface anomalous Hall effect at the interface between two regions with different θ values and no Hall response will exist in the bulk as θ takes a constant value θ_b [53, 54]. The value of θ_b is given by the three-dimensional integration of the Chern-Simons 3-form over momentum space[55, 56]. In addition to the inversion or time-reversal symmetry, θ_b will be quantized with improper rotation symmetries or a combination of time-reversal symmetry and proper rotation symmetries[39, 57]. From Eq. (5), the layer-resolved Hall conductivities in the xy plane is associated with the gradient of θ , $\sigma_{xy}(z) = \frac{e^2}{2\pi h} \partial_z \theta(z)$. Thus the slab Hall conductance (3) is given by the difference of the θ values of bottom and top vacuum $\sigma_{xy}^{slab} = \frac{e^2}{h} \frac{\theta_T - \theta_B}{2\pi}$, which is integer-quantized independent of the θ value of the bulk.

Relation between the θ term and the chiral hinge modes The current carried by the CHMs can be evaluated from the spatial dependent θ , and each chiral hinge channel carries one conductance quantum (e^2/h). We calculate the current through a 2D section disk (D) encircling a

hinge normal to the plane as illustrated in Fig. 2(a), $I = \iint_D d\mathbf{S} \cdot \mathbf{j}_\theta$. The electric field is determined by the gradient of a scalar potential, $\mathbf{E} = -\nabla\Phi(\mathbf{r})$, and we choose the boundary of the disk as an equipotential line Φ_e . By utilizing Stokes theorem, $I = \frac{e^2}{2\pi\hbar} \oint_C d\mathbf{s} \cdot \nabla\theta(\mathbf{r})\Phi(\mathbf{r})$. Thus there is no current or equivalently gapless conducting channel on the hinge when $\theta(\mathbf{r})$ in the two vacuum areas takes the same value $n_1 = n_2$. If they are different $n_1 \neq n_2$, there will be a branch cut separating the two vacuums where $\theta(\mathbf{r})$ is singular. In this situation, the contour integral gives the number of the conducting channels $I/(\Delta\Phi e^2/\hbar) = n_2 - n_1$ which is the winding number of the field $\theta(\mathbf{r})$. $\Delta\Phi = \Phi_e - \Phi_{in}$ denotes the potential difference between the outer contour C_{out} and the inner contour C_{int} . In other words, the gapless hinge mode tracks the singularity of the θ term and vice versa. We also want to emphasize that, even when θ in the bulk is not quantized, the above argument for the gapless chiral hinge channel is still valid.

As show in Fig. 2 (c-f), we plot the layer-resolved Hall responses $\sigma_{\alpha\beta}(r_\gamma)$ ($\epsilon_{\alpha\beta\gamma} = 1$) and the integrated value for $\theta(r_\gamma)$ as a function of the layer index for three directions. In numerical evaluation, we consider a slab geometry with the periodic boundary in the $\alpha\beta$ plane and open boundary condition in r_γ direction. The layer resolved Hall response only distributes near the slab surfaces where θ changes and quickly drops to zero as the position moves into the bulk where θ takes constant value. For the double-loop case in Fig. 2 (c) and (e), the magnetic point group $\tilde{\mathcal{G}}_1$ will put a constraint on the Hall response that the layer-resolved Hall conductivity takes the opposite values for the slab center. Thus the slab Chern numbers vanish for three directions. Due to the presence of the mass term d , the axion angle will deviate from the quantized value π , for example, $\theta_b/2\pi \simeq -0.59$ in Fig. 2 (e). It is also consistent with the symmetry analysis that there is no such symmetry to guarantee the quantization θ_b in $\tilde{\mathcal{G}}_1$. As a consequence, the surface Hall conductance $\sigma_{xy}^B = \frac{e^2}{h}(\frac{\theta_b}{2\pi} - n_z^B)$ for the bottom interface and $\sigma_{xy}^T = \frac{e^2}{h}(n_z^T - \frac{\theta_b}{2\pi})$ for the top interface are not half quantized in sharp contrast to the axion insulators. However, the summation of the surface Hall conductance of the adjacent surface must be quantized since $\sigma_{zx}^i + \sigma_{zy}^j = \frac{e^2}{h}(n_y^i - n_x^j)$ with $i, j = T, B$, indicates whether the hinge mode at the intersection of two surfaces exists or not. For the single-loop case, the symmetry $\tilde{\mathcal{G}}_2$ constrains that the layer-resolved Hall conductivities for z direction are symmetric about the slab center, while for x and y directions are antisymmetric about the slab center. The layer-resolved Hall conductivities in xz plane and yz plane are also related to each other by the \mathcal{S}_4 symmetry. Furthermore, θ_b will be quantized due to the presence of improper rotation symmetry \mathcal{S}_4 and a combination of time-reversal and the diagonal mirror symmetry \mathcal{TM}^{x+y} . As a result, the surface Hall conductance are half-quantized for three directions. In this way, we establish the relation between the the CHMs

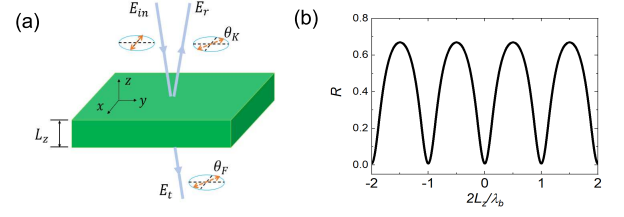


Figure 3. (a) Schematic illustration of the measurement of Kerr and Faraday angle. Incident linearly polarized light becomes elliptically polarized after transmission (Faraday effect) and reflection (Kerr effect), with polarization angles as θ_F and θ_K respectively. (b) The reflectivity R as a function of the slab thickness L_z along z direction in the units of half of photon wavelength $\lambda_b/2$ for suspended single loop case with $\epsilon = 10$ and $\mu = 1$.

and the two physical invariants, $\sigma_{\alpha\beta}^{slab} = \frac{e^2}{h}(n_\gamma^T - n_\gamma^B)$ and $\Delta_{\alpha\beta} = \delta_{n_\beta^T n_\beta^B} \delta_{n_\alpha^T n_\alpha^B} (n_\alpha^T - n_\beta^T)$ with $\epsilon_{\alpha\beta\gamma} = 1$.

Magneto-optical effect as a detection of topological invariants Consider a normally incident linearly x -polarized light with frequency ω propagating along the z direction through the sample $\mathbf{E}_{in} = E_{in} \exp[i(k_0 z - \omega t)]\hat{\mathbf{x}}$ with $k_0 = \omega/c$. \mathbf{E}_r and \mathbf{E}_t are the reflected and transmitted electric field, respectively. Their values at the interface between two materials are related to the incident field \mathbf{E}_{in} by the 2×2 reflection and transmission tensors, and can be solved by matching the electrodynamic boundary conditions. The Kerr and Faraday angles are defined by the $\tan \theta_K = -E_r^y/E_r^x$ and $\tan \theta_F = E_t^y/E_t^x$, respectively[48, 49]. When the chemical potential is located within the surface gap E_g and $\hbar\omega \ll E_g$, the magnetic fields at the interface of the two materials are discontinuous due to the presence of surface Hall current. The reflection and transmission tensors for a slab can be obtained by composing the single-interface scattering matrices for top and bottom surfaces. For simplicity we only consider a free-standing sample, the influence of a substrate do not change our conclusion qualitatively. The reflectivity $R \equiv |\mathbf{E}_r|^2/|\mathbf{E}_t|^2$ will depend on the relative magnitude of the slab thickness and the wavelength ($\lambda_b = \frac{2\pi c}{\omega\sqrt{\epsilon\mu}}$) inside the bulk. When the slab thickness contains an integer multiple of half wavelength $L_z = N\lambda_b/2$ with an integer N (the resonance condition), R reaches the minima. At the resonance, the Faraday θ'_F and Kerr θ'_K rotations have the same universal quantized value [39, 50], $\tan \theta'_F = \cot \theta'_K = \alpha(n_z^T - n_z^B)$, where $\alpha \equiv \frac{1}{4\pi\epsilon_0} \frac{e^2}{\hbar c}$ the fine structure constant. At the resonance, the difference of θ values between the top and bottom vacuum can be obtained irrespective of the specific value of θ_b . In order to determine $n_z^T - \frac{\theta_b}{2\pi}$ and $n_z^B - \frac{\theta_b}{2\pi}$ for top and bottom surface, we also need to use the results at reflectivity maxima when $L_z = (N + \frac{1}{2})\lambda_b/2$. The measured Faraday angle θ''_F and Kerr angle θ''_K give a relation

[39]

$$\tan(\theta''_K + \theta''_F) \left(1 - \frac{\tan \theta'_F}{\tan \theta''_F} \right) = \alpha(n_z^T + n_z^B - \frac{\theta_b}{\pi}).$$

Using the two relations, we can determine the values of the quadrupole indices and the slab Chern numbers.

In short, the quadrupole index in combination with the slab Chern number can determine the flowing pattern of the CHMs, which gives rise to a 3D QAHE in a second order topological insulator.

ACKNOWLEDGMENTS

BF and ZAH are contributed equally. This work was supported by the Research Grants Council, University Grants Committee, Hong Kong under Grant No. 17301220, and the National Key R&D Program of China under Grant No. 2019YFA0308603.

-
- [1] S. M. G. Richard E. Prange, ed., *The Quantum Hall Effect* (Springer-Verlag New York, 1990).
- [2] M. Z. Hasan and C. L. Kane, Colloquium: topological insulators, *Rev. Mod. Phys.* 82, 3045 (2010).
- [3] X.-L. Qi and S.-C. Zhang, Topological insulators and superconductors, *Rev. Mod. Phys.* 83, 1057 (2011).
- [4] S.-Q. Shen, *Topological insulators*, Springer Series of Solid State Science, Vol. 174 (Springer, Heidelberg, 2012).
- [5] D. J. Thouless, M. Kohmoto, M. P. Nightingale, and M. den Nijs, Quantized hall conductance in a two-dimensional periodic potential, *Phys. Rev. Lett.* 49, 405 (1982).
- [6] R. B. Laughlin, Quantized hall conductivity in two dimensions, *Phys. Rev. B* 23, 5632 (1981).
- [7] X.-G. WEN, Theory of the edge states in fractional quantum hall effects, *Int. J. Mod. Phys. B* 6, 1711 (1992).
- [8] Y. Hatsugai, Chern number and edge states in the integer quantum hall effect, *Phys. Rev. Lett.* 71, 3697 (1993).
- [9] C. L. Kane and E. J. Mele, Z₂ topological order and the quantum spin hall effect, *Phys. Rev. Lett.* 95, 146802 (2005).
- [10] L. Fu and C. L. Kane, Topological insulators with inversion symmetry, *Phys. Rev. Lett.* 76, 045302 (2007).
- [11] X. Chen, A. Tiwari, and S. Ryu, Bulk-boundary correspondence in (3+1)-dimensional topological phases, *Phys. Rev. B* 94, 045113 (2016).
- [12] W. A. Benalcazar, B. A. Bernevig, and T. L. Hughes, Quantized electric multipole insulators, *Science* 357, 61 (2017).
- [13] M. Ezawa, Higher-order topological insulators and semimetals on the breathing kagome and pyrochlore lattices, *Phys. Rev. Lett.* 120, 026801 (2018).
- [14] D. Călugăru, V. Juričić, and B. Roy, Higher-order topological phases: A general principle of construction, *Phys. Rev. Lett.* 99, 041301 (2019).
- [15] F. Schindler, A. M. Cook, M. G. Vergniory, Z. Wang, S. S. Parkin, B. A. Bernevig, and T. Neupert, Higher-order topological insulators, *Sci. Adv.* 4, eaat0346 (2018).
- [16] F. Schindler, Z. Wang, M. G. Vergniory, A. M. Cook, A. Murani, S. Sengupta, A. Y. Kasumov, R. Deblock, S. Jeon, I. Drozdov, et al., Higher-order topology in bismuth, *Nat. Phys.* 14, 918 (2018).
- [17] W. A. Benalcazar, B. A. Bernevig, and T. L. Hughes, Electric multipole moments, topological multipole moment pumping, and chiral hinge states in crystalline insulators, *Phys. Rev. B* 96, 245115 (2017).
- [18] Z. Song, Z. Fang, and C. Fang, (d-2)-dimensional edge states of rotation symmetry protected topological states, *Phys. Rev. Lett.* 119, 246402 (2017).
- [19] J. Langbehn, Y. Peng, L. Trifunovic, F. von Oppen, and P. W. Brouwer, Reflection-symmetric second-order topological insulators and superconductors, *Phys. Rev. Lett.* 119, 246401 (2017).
- [20] E. Khalaf, Higher-order topological insulators and superconductors protected by inversion symmetry, *Phys. Rev. Lett.* 97, 205136 (2018).
- [21] M. Geier, L. Trifunovic, M. Hoskam, and P. W. Brouwer, Second-order topological insulators and superconductors with an order-two crystalline symmetry, *Phys. Rev. Lett.* 97, 205135 (2018).
- [22] C. Fang and L. Fu, New classes of topological crystalline insulators having surface rotation anomaly, *Sci. Adv.* 5, eaat2374 (2019).
- [23] L. Trifunovic and P. W. Brouwer, Higher-order bulk-boundary correspondence for topological crystalline phases, *Phys. Rev. X* 9, 011012 (2019).
- [24] C. Yue, Y. Xu, Z. Song, H. Weng, Y.-M. Lu, C. Fang, and X. Dai, Symmetry-enforced chiral hinge states and surface quantum anomalous hall effect in the magnetic axion insulator Bi_{2-x}Sm_xSe₃, *Nat. Phys.* 15, 577 (2019).
- [25] S. H. Kooi, G. Van Miert, and C. Ortix, Inversion-symmetry protected chiral hinge states in stacks of doped quantum hall layers, *Phys. Rev. Lett.* 98, 245102 (2018).
- [26] G. Van Miert and C. Ortix, Higher-order topological insulators protected by inversion and rotoinversion symmetries, *Phys. Rev. Lett.* 98, 081110 (2018).
- [27] E. Khalaf, H. C. Po, A. Vishwanath, and H. Watanabe, Symmetry indicators and anomalous surface states of topological crystalline insulators, *Phys. Rev. X* 8, 031070 (2018).
- [28] J. Kruthoff, J. de Boer, J. van Wezel, C. L. Kane, and R.-J. Slager, Topological classification of crystalline insulators through band structure combinatorics, *Phys. Rev. X* 7, 041069 (2017).
- [29] H. C. Po, A. Vishwanath, and H. Watanabe, Symmetry-based indicators of band topology in the 230 space groups, *Nat. Commun.* 8, 1 (2017).
- [30] S. Ono and H. Watanabe, Unified understanding of symmetry indicators for all internal symmetry classes, *Phys. Rev. Lett.* 98, 115150 (2018).
- [31] H. Watanabe, H. C. Po, and A. Vishwanath, Structure and topology of band structures in the 1651 magnetic space groups, *Sci. Adv.* 4, eaat8685 (2018).

- [32] F. Tang, H. C. Po, A. Vishwanath, and X. Wan, Comprehensive search for topological materials using symmetry indicators, *Nature* 566, 486 (2019).
- [33] F. Tang, H. C. Po, A. Vishwanath, and X. Wan, Efficient topological materials discovery using symmetry indicators, *Nat. Phys* 15, 470 (2019).
- [34] Y. Tanaka, R. Takahashi, and S. Murakami, Appearance of hinge states in second-order topological insulators via the cutting procedure, *Phys. Rev. Lett.* 101, 115120 (2020).
- [35] Y. Tanaka, R. Takahashi, T. Zhang, and S. Murakami, Theory of inversion \mathbb{Z}_4 protected topological chiral hinge states and its applications to layered antiferromagnets, *Phys. Rev. Res.* 2, 043274 (2020).
- [36] R. Takahashi, Y. Tanaka, and S. Murakami, Bulk-edge and bulk-hinge correspondence in inversion-symmetric insulators, *Phys. Rev. Res.* 2, 013300 (2020).
- [37] M. S. Dresselhaus, G. Dresselhaus, and A. Jorio, *Group Theory: Application to the Physics of Condensed Matter* (Springer- Verlag, Berlin, 2008).
- [38] W.-Y. Shan, H.-Z. Lu, and S.-Q. Shen, Effective continuous model for surface states and thin films of three-dimensional topological insulators, *N J. Phys.* 12, 043048 (2010).
- [39] See Supplemental Material at [URL to be added by publisher] for details of Sec. SI. Model Hamiltonian, , Sec. SII. Symmetry of the Hamiltonian, Sec. SIII. Symmetry constraints on quadrupole moments, Sec. SIV. Symmetry constraints on Hall response, Sec. SV. Explicit proof of the quantization of the Chern-Simons invariant, and Sec. SVI. Magneto-optical Faraday and Kerr effects, which includes Refs. [37, 40–42, 49, 55, 56].
- [40] B. Kang, K. Shiozaki, and G. Y. Cho, Many-body order parameters for multipoles in solids, *Phys. Rev. B* 100, 245134 (2019).
- [41] W. A. Wheeler, L. K. Wagner, and T. L. Hughes, Many-body electric multipole operators in extended systems, *Phys. Rev. B* 100, 245135 (2019).
- [42] C.-A. Li, B. Fu, Z.-A. Hu, J. Li, and S.-Q. Shen, Topological phase transitions in disordered electric quadrupole insulators, *Phys. Rev. Lett.* 125, 166801 (2020).
- [43] R.-L. Chu, J. Shi, and S.-Q. Shen, Surface edge state and half-quantized hall conductance in topological insulators, *Phys. Rev. B* 84, 085312 (2011).
- [44] X.-L. Qi, T. L. Hughes, and S.-C. Zhang, Chiral topological superconductor from the quantum hall state, *Phys. Rev. Lett.* 82, 184516 (2010).
- [45] F. Wilczek, Two applications of axion electrodynamics, *Phys. Rev. Lett.* 58, 1799 (1987).
- [46] T. L. Hughes, E. Prodan, and B. A. Bernevig, Inversion-symmetric topological insulators, *Phys. Rev. Lett.* 83, 245132 (2011).
- [47] A. M. Turner, Y. Zhang, R. S. Mong, and A. Vishwanath, Quantized response and topology of magnetic insulators with inversion symmetry, *Phys. Rev. Lett.* 85, 165120 (2012).
- [48] J. Maciejko, X.-L. Qi, H. D. Drew, and S.-C. Zhang, Topological quantization in units of the fine structure constant, *Phys. Rev. Lett.* 105, 166803 (2010).
- [49] W.-K. Tse and A. H. MacDonald, Magneto-Optical Faraday and Kerr Effects in Topological Insulator Films and in Other Layered Quantized Hall Systems, *Phys. Rev. B* 84, 205327 (2011).
- [50] W.-K. Tse and A. MacDonald, Giant magneto-optical Kerr effect and universal Faraday effect in thin-film topological insulators, *Phys. Rev. Lett.* 105, 057401 (2010).
- [51] K. N. Okada, Y. Takahashi, M. Mogi, R. Yoshimi, A. Tsukazaki, K. S. Takahashi, N. Ogawa, M. Kawasaki, and Y. Tokura, Terahertz spectroscopy on faraday and Kerr rotations in a quantum anomalous Hall state, *Nat. Commun.* 7, 12245 (2016).
- [52] V. Dziom, A. Shuvaev, A. Pimenov, G. Astakhov, C. Ames, K. Bendias, J. Böttcher, G. Tkachov, E. Hankiewicz, C. Brüne, et al., Observation of the universal magnetoelectric effect in a 3D topological insulator, *Nat. Commun.* 8, 1 (2017).
- [53] M. Sitte, A. Rosch, E. Altman, and L. Fritz, Topological insulators in magnetic fields: Quantum hall effect and edge channels with a nonquantized θ term, *Phys. Rev. Lett.* 108, 126807 (2012).
- [54] J. Wang, B. Lian, X.-L. Qi and S.-C. Zhang, Quantized topological magnetoelectric effect of the zero-plateau quantum anomalous Hall state, *Phys. Rev. B* 92, 081107 (2015).
- [55] X.-L. Qi, T. L. Hughes, and S.-C. Zhang, Topological field theory of time-reversal invariant insulators, *Phys. Rev. Lett.* 78, 195424 (2008).
- [56] A. M. Essin, J. E. Moore, and D. Vanderbilt, Magneto-electric polarizability and axion electrodynamics in crystalline insulators, *Phys. Rev. Lett.* 102, 146805 (2009).
- [57] C. Fang, M. J. Gilbert, and B. A. Bernevig, Bulk topological invariants in noninteracting point group symmetric insulators, *Phys. Rev. Lett.* 86, 115112 (2012).